Linking warm Arctic winters, Rossby waves, and cold spells: an idealized numerical study

Emilien Jolly, Fabio d'Andrea, Gwendal Rivière, Sebastien Fromang

Linking Warm Arctic Winters, Rossby Waves, and Cold Spells: An Idealized Numerical Study

EMILIEN JOLLY,[a] FABIO D'ANDREA,[a] GWENDAL RIVIÈRE,[a] AND SEBASTIEN FROMANG[b]

[a] *LMD/IPSL, ENS, PSL Université, École Polytechnique, Institut Polytechnique de Paris, Sorbonne Université, CNRS, Paris, France*
[b] *Laboratoire des Sciences du Climat et de l'Environnement, LSCE/IPSL, CEA-CNRS-UVSQ, Université Paris-Saclay, Gif-sur-Yvette, France*

ABSTRACT: The changes of midlatitude Rossby waves and cold extreme temperature events (cold spells) during warm Arctic winters are analyzed using a dry three-level quasigeostrophic model on the sphere. Two long-term simulations are compared: the first run has the observed wintertime climatology, while the second run includes the composite of the global anomalies associated with the six hottest Arctic winters. A spectral analysis shows a large increase in wave amplitude for near-zero and westward phase speeds and a more moderate decrease for high eastward phase speeds. The increase in low-frequency variability (periods greater than a week) associated with the power shift to slower waves is largely responsible for an increase in midlatitude long-lasting cold spells. In midlatitude regions, in the presence of a mean warming, that increase in low-frequency variance compensates the increase of the mean temperature, resulting at places in a frequency of cold spells that remains by and large unaltered. In presence of mean cooling, both the increase in variance and the decrease in the mean temperature participate in an increased frequency of cold spells. Sensitivity experiments show that the power shift to slower waves is mainly due to the tropical anomalies that developed during those particular winters and less importantly to changes in the background flow at higher latitudes associated with the Arctic amplification pattern.

KEYWORDS: Northern Hemisphere; Dynamics; Rossby waves; Extreme events; Winter/cool season; Climate change; Cold air surges

1. Introduction

Observations show that climate warming is not homogeneous over the globe, and Arctic amplification (AA) refers to the accelerated rate of warming of the Arctic near the surface compared to tropics and midlatitudes (Serreze et al. 2009). AA shows a seasonality, with a maximum during late fall and winter (Lu and Cai 2009), it can be found in historical observations, in projection of future climate (Pithan and Mauritsen 2014) and even in paleoclimatic studies (Serreze and Barry 2011), with a consistent relationship with the concentration of greenhouse gases (Fletcher et al. 2019).

Several—nonexclusive—mechanisms of AA have been identified in the literature [see Cohen et al. (2018) for a recent review]. The best-known mechanism is the positive albedo feedback associated with sea ice reduction and snow melting (Screen and Simmonds 2010). Another category of mechanisms of AA involves an increased downward infrared radiation due to changes in cloud cover and water vapor (Graversen and Wang 2009). Intrusions of moisture from lower latitudes might largely be the cause of such changes (Woods and Caballero 2016; Gong et al. 2017; Lee et al. 2017), due to synoptic dynamics in the Arctic (Inoue and Hori 2011; Rinke et al. 2017; Messori et al. 2018) or in lower latitudes (Binder et al. 2017) or due to planetary waves initiated in the tropics (Lee et al. 2011).

The possible influence of AA on midlatitude weather has been the subject of an intense debate during the last decade. In boreal summer, some studies advanced a key role played by Arctic warming in increasing the occurrence of heat waves,

droughts, and flooding events via Rossby waves quasi resonance and changes in jet behavior (Coumou et al. 2014, 2015; Mann et al. 2018). Di Capua and Coumou (2016) found the most robust changes and a significant positive trend in waviness during fall. However, most of the debate is focused on boreal winter, the AA signal is in fact strongest in winter, and there have been concomitant trends of Arctic warming and Northern Hemisphere continents cooling since the 1990s (Cohen et al. 2012b). There have also been specific seasons marked by extreme AA, associated with records in sea ice reduction in autumn followed by extreme cooling over the continents in winter: this was the case of the 2005/06 winter over the Eurasian continent (Petoukhov and Semenov 2010), 2013/14 winter over North America (Lee et al. 2015), and 2009/10 winter over the whole hemisphere (Overland et al. 2011). Finally, some studies detected an increase in the number of cold spells (CS) and noted some record snowfalls in North America, Europe, and Asia over the recent past winters (Liu et al. 2012; Francis and Vavrus 2012; Cohen et al. 2014).

A first category of observational and modeling studies considered a regional influence of sea ice reduction onto the midlatitudes: the Barents–Kara sea ice reduction would imply cold winter over central Eurasia (Honda et al. 2009; Mori et al. 2014) while East Siberian–Chukchi–Bering sea ice reduction would induce cold weather over North America (Kug et al. 2015; Lee et al. 2015). The underlying mechanism is the same, involving the formation of a high anomaly, or high-latitude block, over the reduced sea ice region.

Another category of studies provided evidence for a hemispheric impact and for the formation of the negative phase of the Arctic Oscillation/North Atlantic Oscillation (AO/NAO)

in response to sea ice reduction and/or AA. Such an impact would explain cold continents in winter and favor cold periods over North America and Eurasia (Thompson and Wallace 1998; Yiou and Nogaj 2004). It would also explain that the decades of 1980s and 1990s were marked by an increase in AO/NAO index (Hurrell 1995), while the early twenty-first century has been characterized by near-neutral and negative AO/NAO phases (Overland and Wang 2005; Cohen et al. 2012a). Many studies have also emphasized the key role played by the stratosphere to explain this influence (Cohen et al. 2012a; Peings and Magnusdottir 2014; Nakamura et al. 2015; Hell et al. 2020). While observational studies have emphasized this close relationship between reduced sea ice cover and the negative phase of the AO/NAO, modeling studies have not robustly found the same type of phenomenon (Bader et al. 2011; Cohen et al. 2014; Sun et al. 2016). Finally, it is important to note that such a negative NAO/AO response to Arctic warming, which corresponds to an equatorward shift of the midlatitude jets, can also be found in simple dry atmospheric models without representation of the stratosphere and without land–sea contrasts (Butler et al. 2010; Rivière 2011).

Since the Arctic warming is only one feature of global warming, it is not obvious if its effect will dominate over others. A strong warming is also expected to occur in the tropical upper troposphere, with the effect of shifting the storm tracks and jet streams poleward (Butler et al. 2010; Rivière 2011). The opposite influences of Arctic and tropical warmings is sometimes referred to as the "tug of war" (Barnes and Screen 2015; Shaw et al. 2016). The general effect of global warming in CMIP3 and CMIP5 experiments is mainly characterized by a poleward shift of the jet streams, suggesting that tropical warming influence dominates (Shaw et al. 2016). However, the ability of the models to accurately simulate the spatial heterogeneities of the warming is still questioned (Santer et al. 2018).

The hypothesis has been advanced that Arctic warming would favor large-amplitude meanders of the jet and extreme weather events like CS (Liu et al. 2012; Francis and Vavrus 2012). According to Francis and Vavrus (2012), the phase speed of the waves should decrease because midlatitude westerly jets decrease in intensity in association with the decreased meridional temperature gradient; additionally, the ridges of the waves should become more elongated because of the presence of a positive geopotential height anomaly in the Arctic in connection with the amplified warming. Both effects would induce more amplified and slower-propagating waves and finally more extreme and more persistent temperature events. In particular, this would explain the recent cold and snowy winters. Over Europe, CS are generally induced by the presence of a blocking (Buehler et al. 2011) while over North America large-scale precursors of CS are more associated with amplified slowly propagating wave trains (Grotjahn et al. 2016; Messori et al. 2016; Harnik et al. 2016). However, there is no indication of a positive trend in blocking frequency in reanalysis datasets (Barnes et al. 2014; Davini and D'Andrea 2020), or when detected, they are specific to some regions only (Davini et al. 2012). Furthermore, a decrease in blockings has been detected in CMIP5 and CMIP6 future climate scenarios

(Masato et al. 2013; Davini and D'Andrea 2020). Other studies measured the intensity and the propagation speed of synoptic and planetary waves with different diagnostics but the results are not conclusive (Screen and Simmonds 2013; Barnes 2013; Riboldi et al. 2020), while the sinuosity of the midlatitude flow is projected to decrease in future scenarios of CMIP5 models (Cattiaux et al. 2016).

Extreme temperature events occurrence can be influenced by change in the mean of temperature, its variance, or possibly by higher moments (Tamarin-Brodsky et al. 2019). Screen (2014) showed that the subseasonal cold-season temperature variance has decreased in mid- to high latitudes during recent decades. The same is found in RCP4.5 scenarios of CMIP5 models by Gao et al. (2015) which explain the large decrease in the number and duration of CS. In contrast, Cohen (2016) found a slight increase of variance in midlatitudes from 1989 to 2015. Without changes in the atmospheric circulation, a decrease in the variance is expected simply because southward-advected Arctic air would be less cold (see, e.g., Schneider et al. 2015). Therefore, to potentially get stronger variance in a warming climate circulation changes are necessary.

The impact of AA on the midlatitudes as suggested by Francis and Vavrus (2012) and Liu et al. (2012) lacks strong theoretical arguments, as underlined by Wallace et al. (2014), Barnes and Screen (2015), and Hoskins and Woollings (2015). The present study revisits this hypothesis by analyzing in a simple modeling framework the effect of a decreased temperature gradient on Rossby waves. We use the intermediate complexity model of Marshall and Molteni (1993): a global three-level quasigeostrophic model that has been shown to realistically simulate the wintertime Northern Hemisphere atmospheric circulation, its low-frequency variability (Corti et al. 1997; D'Andrea and Vautard 2001) and its synoptic-scale variability (Drouard et al. 2013; Rivière and Drouard 2015).

Other idealized numerical studies investigated the impact of a decreased temperature gradient on midlatitudes. Using a dry general circulation model, Hassanzadeh et al. (2014) found that a reduced equator-to-pole gradient reduces the wind speed but also blockings and the meridional amplitude of the waves. Based on the results of a hierarchy of models, Ronalds et al. (2018) found that the narrowing of the jet on the poleward flank of its mean position in response to AA leads to a decreased variability of the jet position. Using a zonally homogeneous forcing of the Marshall and Molteni's (1993) model, Robert et al. (2019) showed that a decrease in lower-level baroclinicity makes the latitudinal fluctuations of the jet more persistent.

In the present study, the same model is used but in a more realistic framework with topography, land–sea contrasts and other zonally inhomogeneous forcings. An AA with an amplitude possible for the end of the twenty-first century is included in the model's forcing. Another difference with the previously mentioned studies is that we focus on the changes in Rossby wave propagation and magnitude and their impact on CS.

The basic equations of the model are introduced in section 2, which also includes the setup of two long-term numerical simulations: one *control* run with a climatology close to the

present-day wintertime observations and another forced by Arctic warming. The climatologies of the two runs are analyzed in section 2. In section 3, diagnostics of Rossby wave spectral properties and their differences between the two runs are described. Section 4 is dedicated to changes in CS. In section 5 two additional integrations are analyzed, in order to look at the sensitivity of the response to the latitude of the forcing. Concluding remarks and discussion are provided in section 6.

2. Quasigeostrophic model

a. Model equations

In this work, a version of the global quasigeostrophic (QG) model first introduced by Marshall and Molteni (1993) is used. The model is particularly relevant here as it is the simplest baroclinic model to represent dry Rossby wave dynamics. It integrates the QG potential vorticity (q) equation at three vertical levels:

$$\frac{\partial q_i}{\partial t} = -J(\Psi_i, q_i) - D_i(\Psi_1, \Psi_2, \Psi_3) + S_i, \qquad (1)$$

where the index i indicates the level (1: 200 hPa; 2: 500 hPa; 3: 800 hPa), Ψ is the streamfunction, J is the Jacobian operator, and D_i aggregates all the dissipative terms (a linear drag at the lowest level, a vertical relaxation of temperature and a horizontal diffusion). The source term S_i—or forcing—is the subject of next section. At all times one can transform q into Ψ and vice versa via a linear relationship. Discretized on the three levels, this reads

$$q_1 = 2\Omega \sin\varphi + \nabla^2 \Psi_1 - \frac{\Psi_1 - \Psi_2}{R_{12}^2},$$

$$q_2 = 2\Omega \sin\varphi + \nabla^2 \Psi_1 + \frac{\Psi_1 - \Psi_2}{R_{12}^2} - \frac{\Psi_2 - \Psi_3}{R_{23}^2},$$

$$q_3 = 2\Omega \left(1 + \frac{h}{H}\right)\sin\varphi + \nabla^2 \Psi_3 + \frac{\Psi_2 - \Psi_3}{R_{23}^2}, \qquad (2)$$

where we have introduced the Coriolis parameter $2\Omega \sin\varphi$ (φ is the latitude) and the two Rossby deformation radii ($R_{12} = 700$ and $R_{23} = 450$ km) for the two intermediate layers defined by two adjacent levels. In the lower level, the contribution of orography to the potential vorticity is introduced via the orographic height $h = h(\lambda, \varphi)$, depending on latitude φ and longitude λ, and a height scale H.

From the QG potential vorticity, all other variables can be diagnostically computed. The horizontal wind is obtained from the streamfunction via geostrophy. The temperature is proportional to the thickness of the layers (see appendix for its computation), and is thus defined at 650 and 350 hPa. The model is integrated in the spectral space, after discretization with a triangular truncation of T42.

Since the model temperature is defined at 650 and 350 hPa, the fine-scale structure of AA near the surface is not represented. Our aim being to reproduce the effects of AA on the large-scale meridional temperature gradient at midlatitudes, the use of the present model is, however, justified.
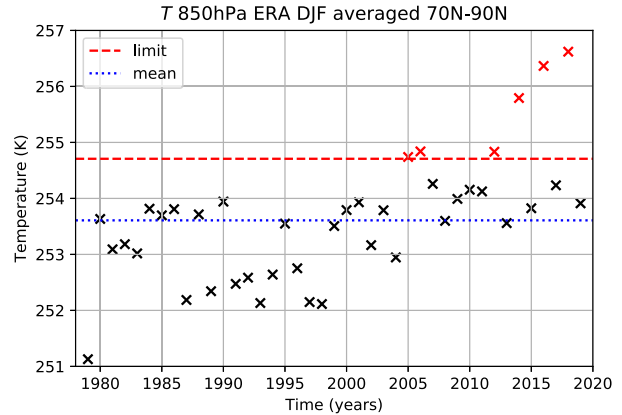

FIG. 1. Time evolution of the average temperature at 850 hPa and between 70° and 90°N every winter (DJF) from 1979 to 2019 (crosses). The blue and red lines correspond to the mean DJF temperature and the sum of the mean and standard deviation, respectively. The red crosses correspond to the six seasons beyond the standard deviation that are taken for the composite of the Arctic amplification pattern.

b. Forcing

The forcing at each of the three levels $S_i = S_i(\lambda, \varphi)$ is a space-dependent and time-constant potential vorticity source, meant to represent the average effect of all the physical processes neglected in the equations. These include diabatic heat sources, linked to precipitations, cloud formation, the interaction with the ocean, etc. and the effect of the divergent flow.

In the original paper of Marshall and Molteni (1993), S_i was determined assuming that the PV tendencies [computed as in Eq. (1)] starting from a large number of observed states have mean equal to zero, which is equivalent to assuming that the large number of observed states is a stable climatology of the model. This procedure can also be seen as an average correction of the model error (D'Andrea and Vautard 2000).

In this work we use the methodology developed by Fromang and Rivière (2020), who applied a variational algorithm to find an optimal S that minimizes the difference between the model climatology and a target one. Here, we used two target climatologies in order to define two different forcing terms.

The control targeted climatology is defined as the wintertime (DJF) ERA-Interim (Dee et al. 2011) streamfunction from 1979 to 2019. The AA targeted climatology is defined using the 6 winters (see Fig. 1) with the highest 850 hPa temperature in the polar cap regions ($\varphi > 70°$N). Among the 6 selected winters, three of them feature a warming in the Barents–Kara Sea region (2004/05, 2005/06 and 2011/12), and three others display warmings centered in other regions: over the Greenland Sea region (2013/14), between the Kara Sea and the nearby continental Siberia (2015/16), over the Bering Strait (2017/18) (not shown). None of these winters present a pan-Arctic warming. The winter 2009/10 is not selected even though it is well known for its warming in the southwest of Greenland (Overland et al. 2011; Cattiaux et al. 2010). Indeed, such a warming mainly occurs at latitudes outside the polar cap region here defined by $\varphi > 70°$N. The streamfunction
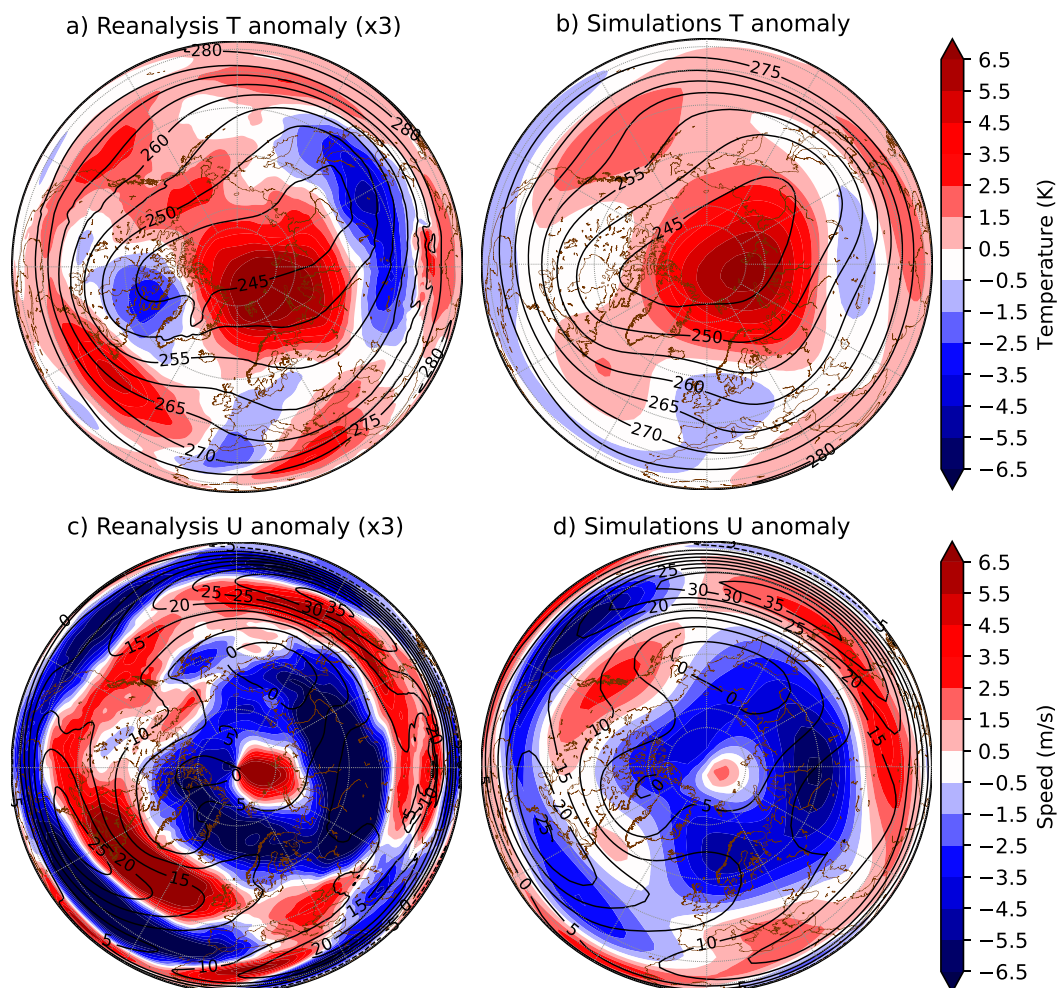
FIG. 2. Ctrl climatologies (contours) and difference between AA and ctrl climatologies (shading) of (a),(b) temperature at 650 hPa and (c),(d) zonal wind at 500 hPa. (a),(c) Triple of the difference between the six strongest AA seasons and the wintertime climatological mean in ERA. (b),(d) Difference between the AA and ctrl simulations.

anomalies of the six chosen winters are averaged, multiplied by 3, and added back to the control targeted climatology. The multiplication by 3 is done to amplify the AA signal. Starting from these two targeted climatologies, two source terms S_{ctrl} and S_{AA} can be defined and are used to force two long-term (100 years of perpetual winter, so 36 500 days) integrations of the model. The ctrl corresponds to the integration with the forcing S_{ctrl}, the AA run to the integration with the forcing S_{AA}. The obtained model climatologies are hereafter called ctrl and AA, respectively.

It is noteworthy that the difference of the two forcing terms (not shown) is not limited to the polar region, even if it is higher in this area. In fact, the variational methods does account for remote forcing effects that optimize the target climatology.

c. Model climatology

The climatology and variability of the model, when forced with the S_{ctrl} and S_{AA} terms defined above are shown and described in the present subsection.

Figure 2 shows ctrl climatologies (black contours) and differences between AA and ctrl (shadings) for the targeted climatologies (left column) and simulations (right column). The targeted and model climatologies have great similarities by construction. Anomalous temperature patterns (Figs. 2a,b) are obviously dominated by the AA, with a high peak centered on the Siberian side of the North Pole (near 80°N, 60°E). Maps of zonal wind at 500 hPa (Figs. 2c,d) show a huge circular decrease around this peak. At lower latitudes, cold and hot anomalies are found, and temperature anomaly, averaged zonally and over the 30°–60°N band, is 0.48 K for the difference between the model climatologies, which matches well with the same value for the difference between the targeted climatologies: 0.40 K.

While the main features of these maps show remarkable correspondences, some differences remain. In the Asian–western Pacific area, a large region of negative temperature anomaly exists in ERA (Fig. 2a) which is also negative in the model but with much smaller amplitude (Fig. 2b). This negative patch over the

a) Low-frequency standard deviation   b) High-frequency standard deviation   c) Percentage of low-frequency in variance
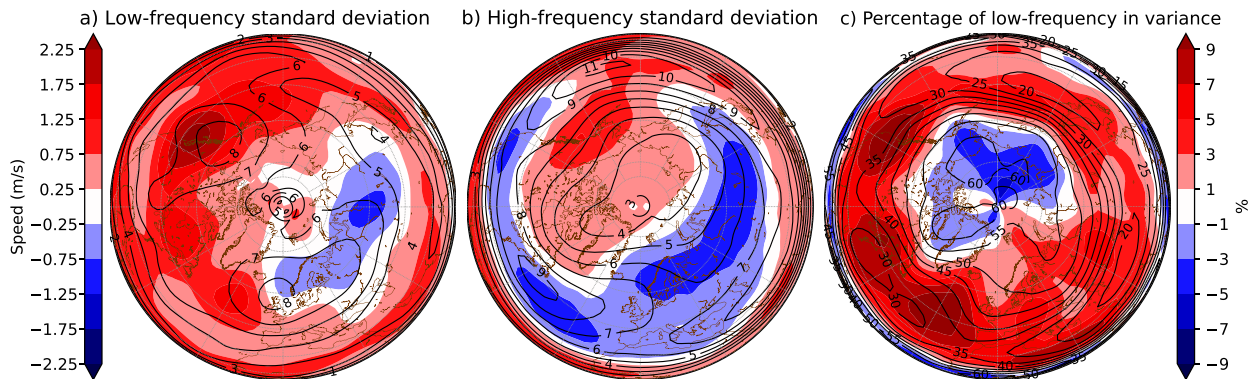

FIG. 3. Standard deviation of (a) low-frequency (periods greater than 10 days) and (b) high-frequency (periods smaller than 10 days) meridional wind at 500 hPa for the ctrl climatology (contours; interval: 1 m s^{-1}) and the difference between AA and ctrl climatologies (shading). (c) Percentage (%) of low-frequency variance in the total variance in the ctrl run (contours) and anomalies of percentage of low-frequency variance between AA and ctrl run (colors).

Eurasian continent has been shown to be related to the sea ice decrease as recalled in the introduction (Honda et al. 2009; Mori et al. 2014). At the same longitudes but farther south, the anomalous temperature is positive which creates anomalous poleward-oriented temperature gradient in eastern Asia. In terms of zonal speed, the anomalous meridional temperature gradient is associated with a northward shift of the western Pacific jet in ERA (Fig. 2c), but with a more intense jet in the simulations (Fig. 2d).

In the eastern Pacific area, the ERA and model climatologies are more similar with a temperature increase mostly everywhere (Figs. 2a,b) leading to a poleward shift of the Pacific jet both in ERA (Fig. 2c) and in the simulations (Fig. 2d).

In the area spanning the American to the European continent, ERA and the simulations show more differences in the temperature maps (Figs. 2a,b). The southern positive temperature spot in the Atlantic is shifted north and the American negative temperature spot is much weaker in the simulation. For the zonal wind (Figs. 2c,d), the dipole of Fig. 2c, leading to a northern shift of the Atlantic jet in ERA is replaced by a decrease in the jet intensity, mainly on its southern flank, in the model. This quite large discrepancy between the targeted anomalies and the model anomalies is due to the iterative process being less successful in converging to the target AA climatology in that region. In the Pacific region, the differences between the targeted and model climatologies are on the same order of magnitude in the AA and ctrl cases.

One unexpected result from the selection of the six most extreme AA seasons is that it clearly shows a poleward shift of both the Pacific and Atlantic jets in ERA. This is surprising because many studies have reported equatorward shifts of the jets and a negative AO phase in response to AA (Cohen et al. 2010; Bader et al. 2011; Barnes and Screen 2015; Yang et al. 2016). As mentioned before, the well-known 2009/10 winter marked by negative AO is not selected because its warming occurs at lower latitude than 70°N. By contrast, our selection picked up the 2013/14 season, which was more characterized by a positive AO (Rivière and Drouard 2015).

In summary, the jets are shifted poleward in ERA, while their intensity is changed in the simulations. In both, however, the zonal wind is reduced on the northern flank of the Pacific and Atlantic jets. The wind anomalies in the model are smaller than the ones in ERA: the decrease in zonal wind around polar regions is -11.8 m s^{-1} in ERA versus -6.3 m s^{-1} in the model, while the maximum value of Arctic amplification is comparable: 6.92 K in ERA against 6.85 K in the model. The changes in U and T in the simulations are 99% significant wherever the anomalies are nonzero using Welch's t test.

In Fig. 3, the standard deviation of the low- and high-frequency meridional wind at 500 hPa are shown. The filter is defined by a seven-point Welch window applied to daily datasets, which has a 10-day cutoff period. Again, the contours correspond to the ctrl case while color shadings report the AA response. The standard deviation changes are 99% significant using a Levene test.

The standard deviations of the low- and high-frequency meridional wind in the ctrl simulation can be compared to those of ERA-I [see, e.g., Fromang and Rivière (2020) for more details]. Two peaks in the standard deviation of the low-frequency meridional wind are present in the ctrl simulation (Fig. 3a), one located in the northeastern Pacific south of Alaska and another one in the northeastern Atlantic north of the British Isles. These peaks, found downstream of the two main storm-track regions shown in Fig. 3b, are roughly located at the same location as in the reanalysis but their amplitudes are weaker (almost one-third reduction compared to ERA-I). Likewise, the high-frequency variability associated with the storm tracks is also less intense than in ERA, especially in the North Atlantic sector.

The difference in low-frequency meridional wind standard deviation between AA and ctrl simulations is generally positive with an enhancement of 0.714 m s^{-1} (12%) in the 30°–60°N band (shading in Fig. 3a). The positive response shows three peaks, two over North America and one in the central North Atlantic. The peak of standard deviation in the northeastern Pacific is stronger in the AA run by 20%, but the peak in the northeastern Atlantic is shifted westward without much change

in its amplitude. The increase in low-frequency variability is not systematic. There is a region with negative anomaly forming a crescent from Scandinavia to a large part of northern Eurasia in the same area where the strongest decrease in zonal wind is observed (Fig. 2d).

The anomalous AA composite of the high-frequency standard deviation (Fig. 3b) is mainly related to the midlatitude jets changes (Fig. 2d). The Pacific storm track intensifies in its western part and then increases on its poleward flank farther east in a similar manner to the westerlies. The Atlantic storm track generally decreases in intensity. This is consistent with a decrease in the intensity of the upper-level Atlantic jet because it is accompanied by a decrease in baroclinicity. Generally speaking, the negative values cover larger areas than the positive ones. There is a well-defined large-scale region of negative values from Scandinavia to northern Eurasia as for the low-frequency variability. However, there are also decreases in high-frequency eddy activity in regions where the low-frequency variability increases: this is the case of the latitudinal band 30°–40°N extending from 140°W to 0°E. In this band the variability shifts from high to low frequency suggesting lower-frequency waves and slower phase speed.

A systematic feature therefore emerges at midlatitudes from Figs. 3a and 3b: the low-frequency contribution to the total variability increases. This is confirmed in Fig. 3c. The total variance, denoted as σ_{tot}^2, is nearly the sum of the variance of the low- and high-frequency meridional wind, denoted as σ_{LF}^2 and σ_{HF}^2, respectively, as the cross covariance between the low- and high-frequency components is small. Hence, $\sigma_{tot}^2 \approx \sigma_{LF}^2 + \sigma_{HF}^2$. Figure 3c presents the percentage of variance explained by the low-frequency component: $100\sigma_{LF}^2/\sigma_{tot}^2$. For the ctrl run (contours), the percentage fluctuates between 20% and 50% at midlatitudes and these regions are logically dominated by storm-track and high-frequency activity. In the polar region, the reverse happens and the transient eddy activity is dominated by the low-frequency component.

Compared to the ctrl case, the AA run shows a systematic increase of the low-frequency contribution to the total variance everywhere at midlatitudes. Even in the Eurasian area, where the low-frequency variance decreases, the high frequency decreases more, so the impact of the low frequency is proportionally higher. In the Arctic, where the part of the low frequency is the highest in the ctrl, the low-frequency contribution slightly decreases in the AA run.

Another result emerges from Figs. 3a and 3b: as first noted by Hassanzadeh et al. (2014), the total variance varies in tandem with the zonal wind. The high- and low-frequency variances (and thus the total variance) increase where the zonal wind strengthens (south of Alaska) and decrease where the zonal wind weakens (Eurasia). The spatial correspondence with the zonal wind anomalies tends to be more obvious for the high-frequency variance, which probably comes from the close relationship between baroclinicity and storm-track activity as emphasized above.

To conclude, the most original result brought out by this section is an increased percentage of variance explained by the low-frequency component at the expense of the high-frequency component at midlatitudes. That result is further detailed and interpreted in the following section.

3. Rossby wave response

a. Space–time spectral analysis

Hayashi (1971) has introduced a spectral analysis of space–time variability for geophysical variables on a latitude circle. Rather than a usual spectrum with the frequency ω in abscissa and the dimensionless zonal wavenumber m in ordinate, in this spectrum the direction of propagation is included. Particularly, in Hayashi (1979), ω is replaced by the phase speed c_ϕ, which is negative in the case of westward waves. Hayashi (1982) proposed to separate the field between transient and standing (stationary) waves, the last being the sum of westward and eastward waves having the same speed and phase.

The power density spectrum is operationally computed as presented by Dell'Aquila et al. (2005, see their appendix) but using the meridional wind rather than the geopotential height. The first step is the Fourier analysis of the spatial field, and the second is a time power spectrum of each wavenumber. Then the dependency to phase speed is found using $c_\phi = \omega/k = (\omega a \cos\varphi)/m$, where k is the dimensional zonal wavenumber, m the dimensionless zonal wavenumber, and a the Earth radius. Here, Hayashi spectra are computed with meridional wind at 500 hPa and finally averaged over the latitudinal band 35°–65°N.

An alternative method to visualize the spectral characteristics of the signal is the phase speed–amplitude histogram. Here the model is run for 10 years with a sampling frequency of 6 h instead of 1 day to get accurate computation of the phase speed. By applying a fast Fourier transform (FFT) to the latitude-averaged meridional wind, we get the amplitude and the phase ϕ for each wavenumber and time. The phase speed is computed as follows:

$$c_\phi = \frac{\omega}{k} = \frac{a\cos\varphi\,\Delta\phi}{m\Delta t}, \qquad (3)$$

where Δ represents a centered scheme difference with 6-hourly outputs.

b. Results

Figure 4 shows the Hayashi spectrum of the ctrl simulation (contours), and the difference of spectrum between the AA and ctrl simulations (colors). For synoptic wavenumber range (5–9) the ctrl spectrum shows high power for eastward-traveling waves. At smaller wavenumbers (less than 4), the power peaks near the zero phase velocity. For wavenumbers 3 and 4, the power is still stronger for eastward-traveling waves than westward-traveling waves while for wavenumber-1 and -2 westward-traveling waves have power as high as the eastward-traveling waves. In general, these features compare well with observed spectrum (see Dell'Aquila et al. 2005, and references therein) and testify that the QG simulations have realistic Rossby wave dynamics.

The difference between the AA and ctrl simulations shows an increase of power for negative and zero phase speeds, which
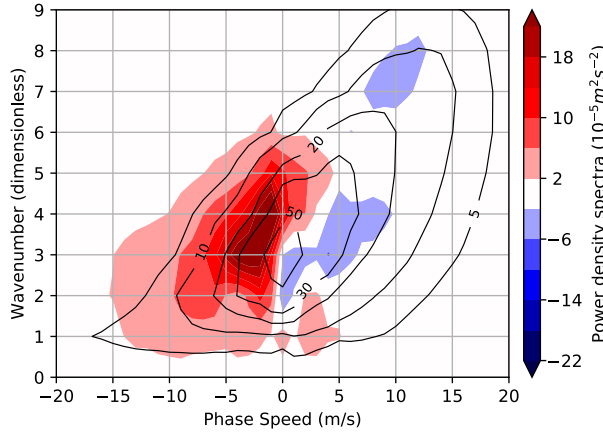
FIG. 4. Latitudinal average (35°–65°N) of the Hayashi spectra of meridional wind at 500 hPa in the model. Contours indicate the ctrl run (contours between 5 and 100 × 10⁻⁵ m² s⁻²). Colors indicate the difference between the AA and ctrl runs.

is particularly strong for wavenumbers 3–5, and a small decrease in power for positive phase speeds. In particular, the power of quasi-stationary waves for wavenumbers 4 and 5 has increased by nearly 50%, while that of modes with wavenumbers 2 and 3 has been reduced. This shift toward higher wavenumbers is expected from Hoskins and Woollings's (2015) argument based on the stationary Rossby wave barotropic formulation and its dependence on zonal wind.

Phase speed–amplitude histograms are shown in Fig. 5. Histograms of the ctrl simulation are in agreement with the Hayashi spectrum of Fig. 4: waves travel more and more rapidly eastward for higher wavenumber. For wavenumbers 1–3 the peak of the histogram is close to zero, i.e., the waves are mostly stationary. For higher wavenumber, the peak moves more and more to the positive phase speed side (between 0 and 5 m s^{-1} for $m = 3$–5 and 5–10 m s^{-1} for $m = 6$–8).

Differences between AA and ctrl runs exhibit dipolar anomaly patterns for all wavenumbers. There are more cases with near-zero or even negative phase speed and less cases with positive phase speed in presence of AA for all wavenumbers except for $m = 1$ which is not very energetic. Again in agreement with the Hayashi spectrum, wavenumbers 3–5 gain power through an increase in the number of high-energy days with near-zero phase speed, while decreases in frequency are for eastward or low-amplitude waves. The negative and positive anomalies for eastward and westward phase speed, respectively, are more symmetric in the histograms than in the Hayashi spectrum. The latter is indeed more dominated by the increase in power of near-zero and negative phase speed modes. This can be understood by the fact that the increased number of days generally corresponds to high-amplitude waves with high power while the decrease corresponds to low-amplitude waves whose impact on the power is much smaller.

In summary, the two diagnostics give coherent results, showing an increase of westward and quasi-stationary waves in number and in power, and a decrease of eastward waves, particularly for long waves with wavenumbers 3–5.

c. Interpretation using the barotropic Rossby wave dispersion relation

To understand the decrease in phase speed at midlatitude, we use the barotropic dispersion relation of a linear Rossby wave evolving along a zonal background flow slowly varying in the meridional direction y:

$$c_\phi = U - \frac{\beta - \frac{\partial^2 U}{\partial y^2}}{k^2 + l^2}, \tag{4}$$

where k and l are zonal and meridional wavenumbers, and U the background zonal wind. Such a relation has been extensively used to study the meridional propagation of Rossby waves in general (Hoskins and Karoly 1981; Held 1983; Hoskins and Ambrizzi 1993) and more recently in the context of the impact of polar amplification on midlatitudes (Ronalds et al. 2018). Here, our purpose is to use this relation to attribute changes in the phase speed for a given k to specific terms of the equation. For a given k, the difference in phase speed between the AA and ctrl runs Δc_ϕ can be expressed at first order as

$$\Delta c_\phi = \Delta U - \frac{\Delta\left(\beta - \frac{\partial^2 U}{\partial y^2}\right)}{k^2 + l^2} + \frac{\beta - \frac{\partial^2 U}{\partial y^2}}{k^2} \frac{\Delta\left(\frac{l^2}{k^2}\right)}{\left(1 + \frac{l^2}{k^2}\right)^2}. \tag{5}$$

The first term on the right-hand side of the equation corresponds to changes in the mean wind, the second term to changes in the absolute vorticity gradient, and the third term to changes in the meridional wavenumber l.

The first and second terms of the right-hand side of Eq. (5) can be readily computed from changes in the climatological means of the zonal wind and absolute vorticity gradient (Figs. 6a,b). The background zonal wind U is thus averaged over time and longitude but also vertically averaged over the three levels of the model. The ratio l/k is estimated by computing the ratio of the standard deviation of the zonal and meridional geostrophic wind components: $l/k = \sqrt{\sum(u_k - \overline{u}_k)^2}/\sqrt{\sum(v_k - \overline{v}_k)^2}$, where u_k and v_k denote the zonal and meridional geostrophic wind components of a given k, respectively. The bars correspond to the time mean. All the terms of Eq. (4) averaged over boxes of 15° in latitude are shown in Figs. 6c and 6d.

The increase in temperature in the polar cap region decreases the zonal wind on the northern flank of the jet, north of 55°N (Figs. 6a,b). This decrease occurs in both ERA (with the anomalies multiplied by 3) and simulations. At lower latitude, ERA and simulations show more differences, consistently with our previous comments on Fig. 2: in ERA (Fig. 6a), the jet is shifted northward with AA whereas not much difference is detected in the simulations, apart a very slight decrease in amplitude. In both ERA and simulations, however, the zonal wind decrease on the poleward flank of the jet makes the jet thinner.

The different terms of Eq. (5) are shown in Figs. 6c and 6d, computed for zonal wavenumber $m = 5$ and for the different latitudinal bands. The first term of Eq. (5), associated with
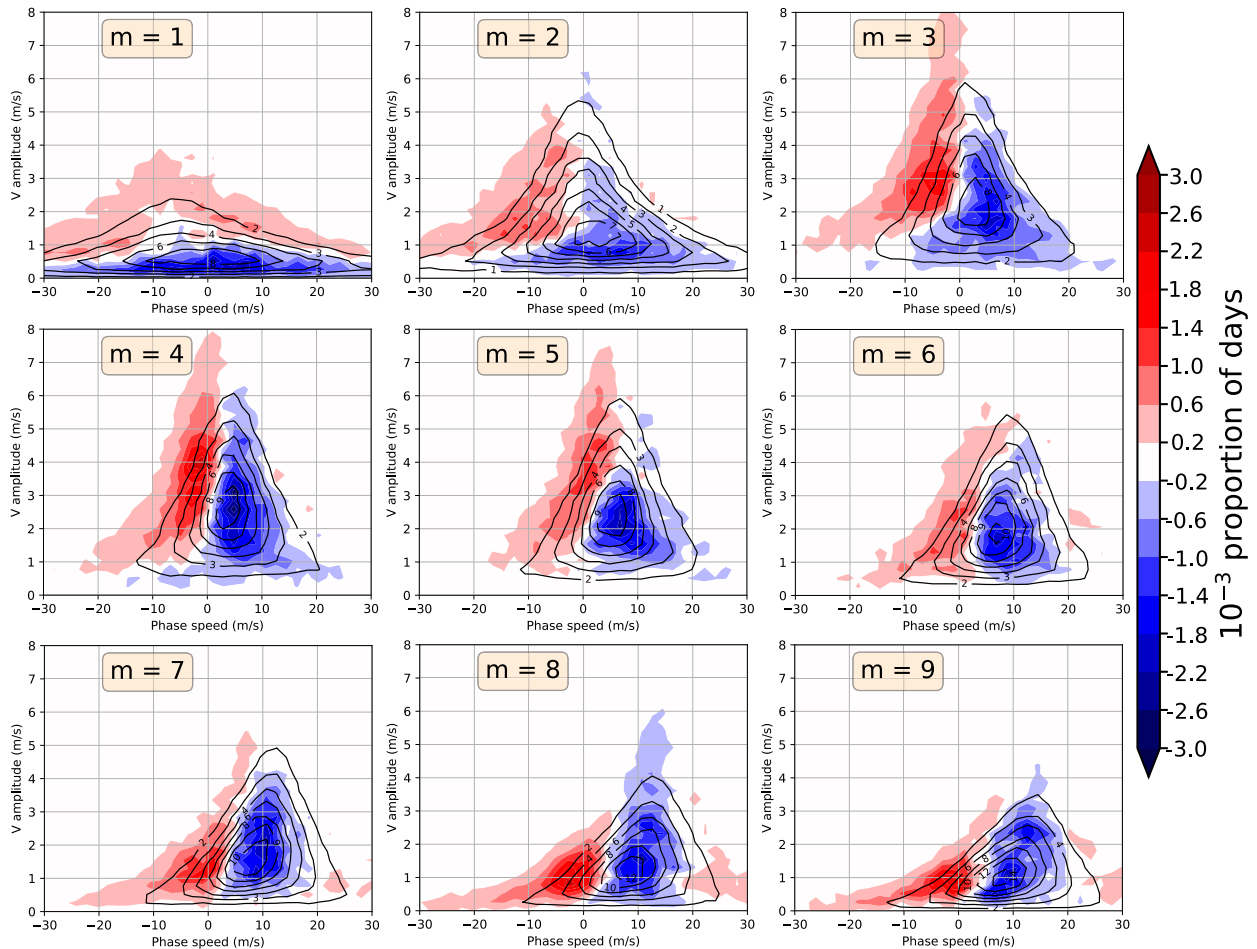
FIG. 5. Phase speed–amplitude histograms of meridional wind at 500 hPa in the model for the first nine zonal wavenumbers. Contours indicate the ctrl run (contours between 1 and 15×10^{-3}). Colors indicate the difference between the AA and ctrl runs.

zonal wind decrease, appears to be the main driver of the phase speed variations at high latitudes (see the blue bars for latitudes greater than 50°N). The second term of the equation is linked to changes in the absolute vorticity gradient, or the second derivative (i.e., the convexity) of the zonal wind. For lower latitudes (in the band from 35° to 50°N), as zonal wind decreases on the northern flank of the jet, the jet becomes thinner, so the absolute vorticity gradient increases in the jet-core region. This makes the second term of Eq. (5) negative and has the effect of reducing the phase speed. In ERA, the second term completely offsets the increase of zonal wind in the latitudinal band 35°–50°N, and consequently the phase speed is reduced. In the simulations, the second term is also negative, although less strongly than in ERA, but its net effect, in conjunction with the third term, is also a decrease in phase speed. The third term of the equation is linked to changes in meridional wavenumber for a given zonal wavenumber. Smaller l values correspond to more meridionally elongated eddies. In the band 35°–50°N, the decrease of l contributes to the phase speed decrease for both reanalysis and simulations.

Finally, south of 35°N, the models and the reanalysis behave differently: there is no net change in the model while the reanalysis exhibits an increase in the phase speed according to

the considered barotropic framework. It is important to emphasize that changes of the perturbation elongation Δl cannot be directly related to the Francis and Vavrus (2012) argument about the elongation of the jet meanders. Indeed, Δl measures the change in the perturbation meridional extension where the perturbation is defined as the deviation from the time mean, so here the effects of the modified time mean flow on the transient perturbation is estimated. Francis and Vavrus (2012) considered the time mean flow anomaly as a part of the perturbation to explain the increased meridional extension of the jet meanders: they did not consider the potential change of the transient perturbation itself.

The above results are shown for wavenumber 5, but similar results are obtained for zonal wavenumbers 3–8 (not shown): phase speeds are found to decrease at midlatitudes (35°–65°N). The comparative impact of the three terms discussed above, however, changes with wavenumber. Higher wavenumbers are more strongly affected by zonal wind changes while lower wavenumbers are more largely influenced by PV gradient or meridional elongation changes.

To conclude, in both reanalysis and simulations, the change in synoptic Rossby wave phase speed at high latitudes is dominated
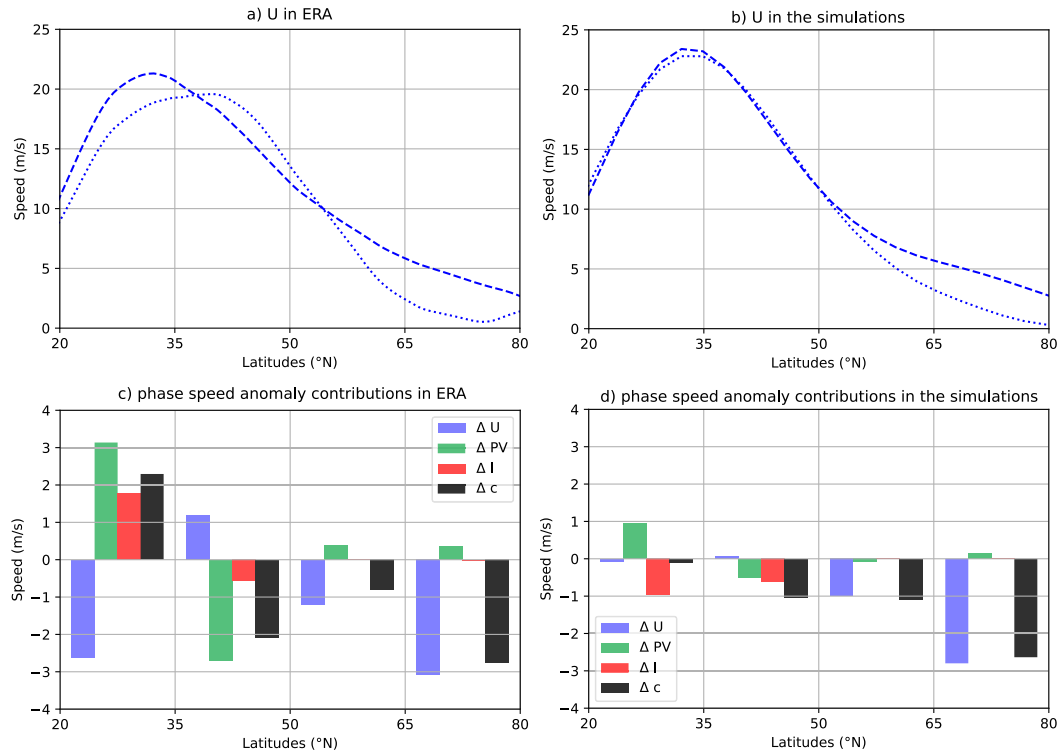
FIG. 6. (a),(b) Zonal-mean zonal wind averaged from 800 to 200 hPa as function of latitude. (a) ERA-Interim: the dashed curve represents the 1979–2017 climatology and the dotted curve corresponds to the AA composite climatology, for which the differences with the 1979–2017 climatology has been tripled. (b) The dashed and dotted curves represent the climatologies of the ctrl and AA simulations, respectively. (c),(d) Phase speed changes due to the zonal wind (ΔU, blue), absolute vorticity gradient (ΔPV, green), meridional wavenumber (Δl, red) terms involved in the barotropic dispersion relation for zonal wavenumber 5. The sum of the terms is Δc in black. The limits in latitude of the averaging boxes are indicated on the x axis.

by the change in zonal wind, while at lower latitudes, near the jet core, it is more impacted by the variations of the absolute vorticity gradient or the meridional elongation. At all latitudinal bands, the net effect is a decrease in phase speed according to the barotropic dispersion relation. Even though the change in the eddy elongation is not explained, the effect of AA on the background zonal wind and absolute vorticity gradient, explained by the narrowing of the jet, provides an interpretation for the slowing down of Rossby waves.

4. Cold spells

In this section, the impact of variability and wave activity changes in the model on extreme phenomena is examined by focusing on CS. A CS is here defined as an episode of at least 5 consecutive days below a temperature threshold depending on the geographical position. At each grid point the threshold is established as the 10th percentile of the temperature distribution of the ctrl simulation.

In the ctrl run, there is a large number of CS in the polar region, with more than 200 CS in total during the 100 years of the run (contours in Fig. 7a). Minima are found at midlatitudes in the Pacific and Atlantic areas, with less than 40 CS. This is linked to the storm tracks, so that temperature anomalies tend

to be short lived, while CS duration is at least 5 days by definition. The number of CS slightly increases over continents compared to the ocean basins to reach values of around 100 CS over North America, Europe, and Asia.

Anomalies in the AA run are dominated by a mean decrease of 60% in CS in the Arctic region (60°–90°N). In midlatitudes, the frequency of CS increases in three areas: North America, western Europe, and central Asia. This map closely resembles the mean temperature anomalies spatial distribution (Fig. 2b): a locally hotter or colder mean temperature obviously influences the probability of exceeding the threshold. This is reflected in the correlation coefficient between the two maps, which is equal to −0.89.

In Fig. 7b, the mean duration of CS is computed as the number of days in cold spells divided by the number of cold spells. CS always last more than 5 days by definition, but are shorter in the storm tracks and last longer in the polar region. The changes in CS duration are related to changes in CS number, with a large decrease at high latitude and an increase at midlatitudes (0.1 days in average). In some midlatitude regions, the increase is large as in the Atlantic sector where the low-frequency variance is strong too (Fig. 3a).

We can separate the effect of the mean and the effect of the variability by subtracting the mean temperature difference to the AA temperature datasets before applying CS definition, and by applying the same standard deviation to both time
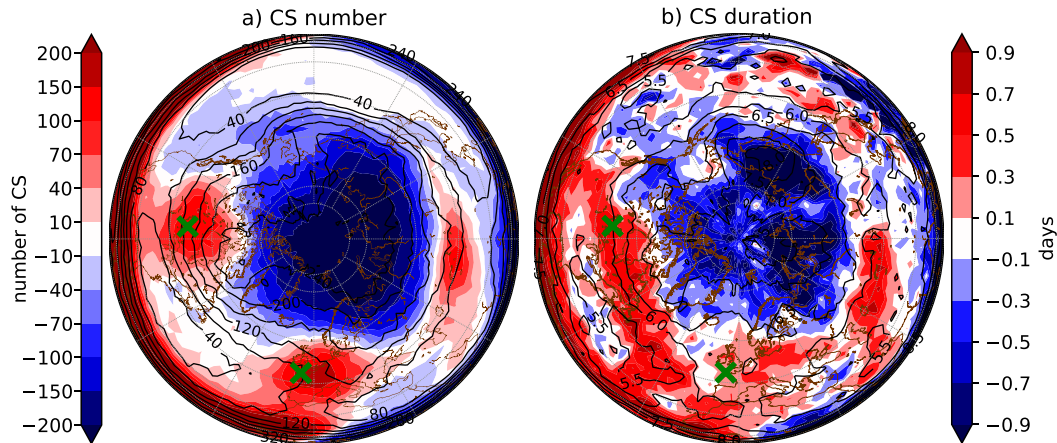
FIG. 7. (a) Number of CS for the ctrl simulation of 100 years (contours; dimensionless) and difference between AA and ctrl runs in the number of CS (shading; dimensionless). (b) As in (a), but for the duration of CS (time in days). The crosses refer to the localization of the grid points developed in Table 1.

series (for each grid point), respectively. This leads to the definitions of two new temperatures

$$T_{=\text{mean}} = T_{\text{AA}}(\lambda, \varphi, t) + \overline{T}_{\text{ctrl}}(\lambda, \varphi) - \overline{T}_{\text{AA}}(\lambda, \varphi), \qquad (6)$$

$$T_{=\sigma} = [T_{\text{AA}}(\lambda, \varphi, t) - \overline{T}_{\text{AA}}(\lambda, \varphi)] \frac{\sigma[T_{\text{ctrl}}(\lambda, \varphi, t)]}{\sigma[T_{\text{AA}}(\lambda, \varphi, t)]}$$
$$+ \overline{T}_{\text{AA}}(\lambda, \varphi), \qquad (7)$$

where σ stands for the standard deviation. The number of CS defined as the number of episodes for which $T_{=\sigma}$ (resp. $T_{=\text{mean}}$) is below the 10th percentile of the temperature distribution of the ctrl simulation for at least 5 consecutive days is shown in Fig. 8a (resp. Fig. 8b). When the influence of the standard deviation on the definition of CS is removed (Fig. 8a), the impact of the changes in the mean temperature is highlighted by comparing Figs. 8a and 8c. The correspondence between Figs. 8a and 8c is compelling and it increases with respect to the full response shown in Fig. 7a. The correlation coefficient slightly increases to −0.91.

In Fig. 8b, the contributions of the higher moments of the temperature distribution to the CS can be assessed. When the differences in the mean are suppressed, smaller differences between the AA and ctrl simulations appear in the polar cap region, and the link with the low-frequency temperature standard deviation (shown in Fig. 8d) appears: the correlation coefficient is 0.83. The three regions of particular increase in CS number in this map, which are the North Pacific, North America, North Atlantic, correspond to regions of important increase in the low-frequency temperature standard deviation. Conversely, the crescent-shaped region of decrease in the number of CS between Scandinavia and Siberia corresponds to a region where the low-frequency temperature variability decreases (Fig. 8d), as has been already discussed in section 2c. Because of the condition on the minimal duration of CS (5 days), CS without the mean (Fig. 8b) fits better with changes in the low-frequency variability than with the total variability. Indeed, the correlation with the total standard deviation (not shown) is 0.76 and less than with the low-frequency component (0.83). This is particularly true in the band 30°–40°N extending

from the eastern Pacific to the eastern Atlantic where there is no increase in the total variability but an increase in both the low-frequency variability and the number of CS.

It appears clearly that the increased variability can locally counterbalance the mean temperature increase and even offset it completely locally, particularly in the midlatitude band. For instance, over continental North America the mean temperature difference of the two simulations is near zero (Fig. 8c), but there are more CS (Fig. 7a) because the low-frequency variability increases (Fig. 8d) and causes long events of polar air advection toward the United States.

For illustrative purposes, we now focus on two particular regions in the NH: one in western Europe and one in the North American Midwest, marked by the two green crosses. Mnemonically we can identify them with Brest, France, and with Winnipeg, Manitoba. For both locations, we report in Table 1 the changes in the total number of CS and the changes following the definitions of Eqs. (7) and (6). These estimates are obtained as follows. If one takes the example of Winnipeg, there are 138 CS in the ctrl simulation, and 278 CS in the AA simulation, hence an increase of 140 CS is reported in Table 1 (cf. also with Fig. 7a). Without the influence of the mean temperature change, i.e., using Eq. (6), we found 241 CS in the AA simulation (Fig. 8a), hence an increase of 103 CS compared to the ctrl run (fourth column in Table 1). To summarize, the total change is 140 CS in the AA run, of which 103 CS are not due to the mean. Making the hypothesis that all the others, i.e., 140 − 103 = 37 CS, are due to the mean change, we attribute 26% of the CS number increase to the mean temperature change. Applying the same line of reasoning when using Eq. (7), we found that 60% of the changes of CS in Winnipeg are due to the variance increase. We applied the same method for Brest, where we found that it is more the change in the mean (50%) than the variability (17%) that matters most for the CS increase at that location.

Table 1 also shows the mean duration of CS. In Brest, the mean duration of CS increases by 0.2 days, In Winnipeg, it extends by 0.5 days. While in Brest the change of duration is due to the mean decrease of temperature, in Winnipeg its impact appears to be minimal.
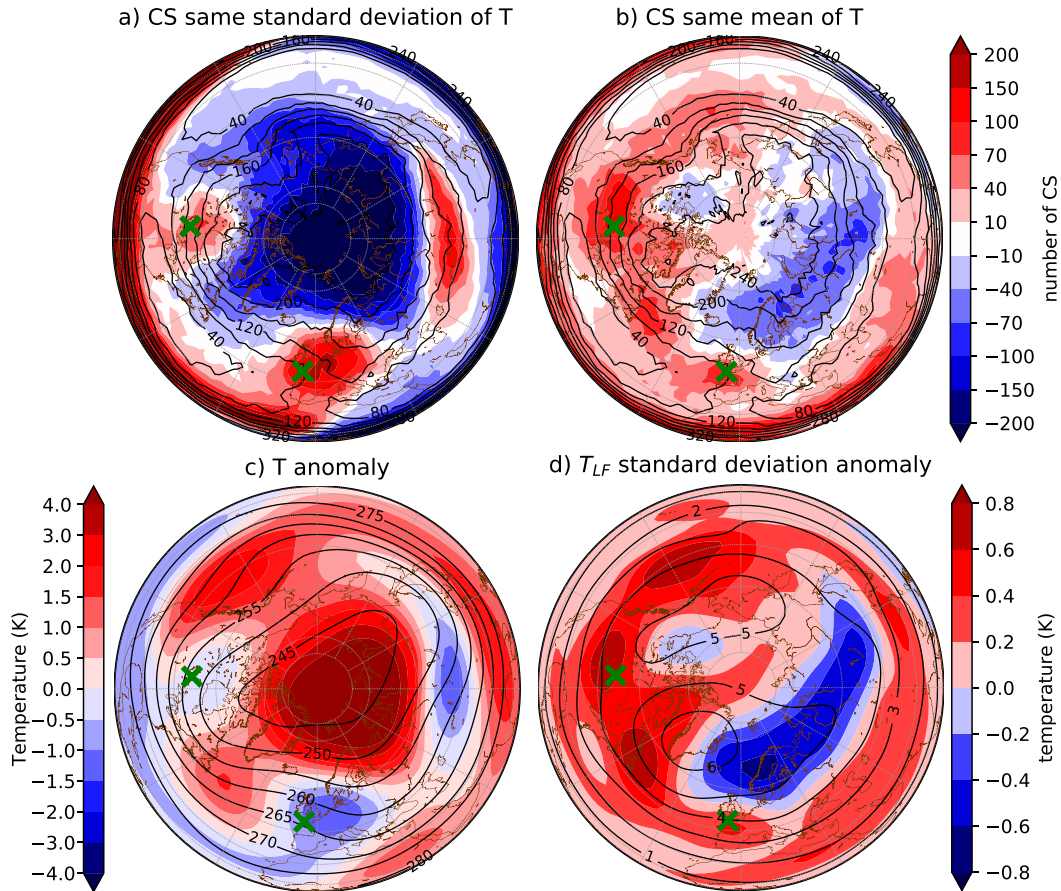
a) CS same standard deviation of T   b) CS same mean of T

c) T anomaly   d) T_{LF} standard deviation anomaly

FIG. 8. (a) As in Fig. 7a, but with T_{AA} data having the same standard deviation as T_{ctrl} [see Eq. (7)]. (b) As in Fig. 7a, but with T_{AA} data translated to the same mean as T_{ctrl} [see Eq. (6)]. (c) Difference in mean temperature at 650 hPa between the AA and ctrl simulations (colors) and mean of T_{ctrl} (contours; units: K). (d) Difference in standard deviation of low-frequency T at 650 hPa between the AA and ctrl simulations (colors) and standard deviation of low-frequency T_{ctrl} (contours; units: K).

In summary, changes in mean temperature dominates the changes of CS, but the response to AA can balance these modifications in some areas where the changes in low-frequency temperature standard deviation are large, and where changes in the mean are consequently overwhelmed by standard deviation increase. This is, for example, the case over North America. It is worth noting that individual CS events last also, on average, longer at midlatitudes in presence of AA. Both the increase in the number of CS (as defined with a minimum duration of 5 days) and the increased duration of CS in presence of AA are attributed to an increase in low-frequency variability in close connection with a slowing down of the eastward propagation of Rossby waves.

5. Sensitivity to tropical and extratropical regions

To assess the relative importance of the different regions in setting up the changes in Rossby wave spectra and CS statistics in the AA run compared to the ctrl run, two additional 100-yr-long simulations were performed. To do so, two forcing S were calculated using the iterative method described in section 2: for

the first one, referred to as the "extratrop" simulation, the target climatology corresponds to the control target climatology south of a latitude of 35°N, but to the AA target climatology for latitudes larger than 35°N. The choice of this particular latitude is made following Fig. 6, which shows that the latitudinal band 35°–50°N matters in our interpretation of the phase speed decrease. For the second simulation, referred to as the "trop" simulation, the target climatology is set to the control target climatology, except for latitudes between 35°S and 35°N where it corresponds to the AA targeted climatology. If we discard the influence of the Southern Hemisphere south of 35°S and expect a linear response for the two runs, their sum should provide the AA run.

The temperature anomalies of the two simulations with respect to the ctrl run are shown in Figs. 9a and 9b. As expected, the extratrop simulation exhibits a warming pattern at high latitudes centered between the North Pole and Siberia of the same amplitude as in the AA simulation (cf. Fig. 9a with Fig. 2b). In midlatitudes, the extratrop simulation patterns display fewer similarities with the AA run, which might be due to the closeness with the transitional latitude 35°N.

TABLE 1. For the two locations identified by a green cross, the number of CS in the ctrl simulation (Fig. 7a, contours), the difference in the number of CS between the ctrl and the AA simulation (Fig. 7a, colors), when the mean in the same (Fig. 8b, colors), and when the standard deviation in the same (Fig. 8a, colors), percent of the change due to the mean and the standard deviation, and changes in mean temperature (Fig. 8c, colors) and temperature standard deviation (Fig. 8d, colors). The last columns compare CS durations for ctrl and AA runs (Fig. 7b) and when the mean is the same.

	CS No.	Change of CS			Due to		Anomaly (K)		CS duration (days)		
Position	Ctrl run	Total	Same mean	Same std	Mean	Std	Mean	Std	Ctrl	AA run	Same mean
Brest	79	+159	+80	+132	50%	17%	−1.01	+0.25	6.44	6.64	6.43
Winnipeg	138	+140	+103	+56	26%	60%	−0.34	+0.64	5.99	6.53	6.49

As expected from the minimization algorithm, the trop simulation exhibits less strong anomalies than the extratrop simulation at high latitudes. However, the anomalies are not small and there is a warming pattern centered over the pole (Fig. 9b) whose peak amplitude is half that of the AA or extratrop runs. It shows that, despite the minimization procedure which tends to avoid any anomalies with respect to the ctrl simulation at high latitudes, the model forms anomalies with a clear Arctic warming pattern from the sole knowledge of tropical anomalies. It supports the recent findings of Baggett and Lee (2017) and Gong et al. (2020), for instance, who showed that planetary-scale Rossby wave trains triggered by anomalous tropical convection in the western Pacific are responsible for setting the Arctic warming patterns.

Hayashi spectra for the two sensitivity experiments are shown in Fig. 10. The spectrum of the extratrop simulation exhibits a dipolar anomaly corresponding to a shift toward smaller—or more negative—phase velocities, which is more obvious for wavenumbers 3 and 4 (Fig. 10a). This shift toward lower frequencies corroborates the interpretation provided in section 3c. The spectrum of the trop simulation is similar to the AA run with increased energy for near-zero and westward phase speed (cf. Figs. 10b and 4). It means that the mean tropical anomalies are responsible for an increased activity of the slowly and slightly westward-propagating waves at midlatitudes. An interpretation for such a behavior would need further analysis and is not provided here. Finally, the two latitudinal bands participate in the energy spectra of the AA run but the trop simulation brings more similarities with the latter run.

CS statistics for the two simulations are shown in Fig. 9. As for the AA run, the change in CS number is dominated by the change in the mean temperature (Figs. 9c,d). By subtracting the mean temperature difference as in Eq. (6), the CS number largely increases in midlatitudes in the trop simulation as in the AA run but more importantly in the Pacific than in the Atlantic while the reverse happens for AA run (see Figs. 9f and 8b). For the extratrop simulation, there is some increase in CS number in a narrow latitudinal band between 30° and 50°N but farther north the decrease is rather systematic in all the regions.

To conclude, it is the trop simulation rather than the extratrop simulation that brings more similarities with the AA run in terms of change in CS number and change in energy spectra. The net increase in near-zero and small westward phase speed in the trop simulation provides an explanation for the increased CS number in midlatitudes when the mean temperature is the same as in ctrl. Yet the reason for such an increased amplitude for slow westward phase speed remains an open question that would need further analysis.

The extratrop simulation exhibits a more moderate increase in CS number in a narrower latitudinal band that can be explained by the shift from high to low frequencies resulting from the background flow changes according to section 3c. But it seems of secondary importance relative to the signal coming from the tropics.

6. Discussion and conclusions

In this article, a dynamical mechanism linking Arctic amplification and Rossby wave dynamics has been studied using a simple, quasigeostrophic model. The link to the frequency and intensity of cold spells has also been addressed. While a comprehensive theory on the wave response to the northern midlatitude to AA is still missing (Hoskins and Woollings 2015), advances have recently been obtained by the use of such highly idealized models. For instance, the reduction of the hemispheric meridional temperature gradient has been shown to reduce the frequency of blocks (Hassanzadeh et al. 2014) and to increase the persistence of the leading mode of variability of midlatitude jets (Robert et al. 2019). We meant here to bring the level of model complexity one step further and introduce longitudinal details (continents, orography), and account for the fact that AA does not really determine a latitudinally uniform temperature gradient reduction.

Our strategy was to compare two runs, one serving as a reference and another one where anomalies corresponding to warm Arctic winters are imposed everywhere over the globe. Differences in terms of Rossby waves properties and cold spells are then analyzed. The imposed anomalies cause a reduction of planetary and synoptic Rossby wave phase speed at midlatitudes. Such changes are in agreement with changes in the variances of temperature and wind for different frequency bands: high-frequency variability (periods smaller than a week) mainly decreases while low-frequency variability (periods larger than a week) increases.

The slowing down of Rossby wave phase speed can be interpreted using the barotropic Rossby wave dispersion relation and background flow anomalies at mid- and high latitudes. The polar increase of temperature above 60°N weakens the zonal wind at those latitudes, which correspond on average to the northern flank of the jet. This makes the jet thinner, which changes the meridional PV gradient as a result. Both these effects decrease the phase speed of Rossby waves, the first being dominant above 60°N and the second just south of it, closer to the jet core. Such an interpretation is confirmed when only anomalies north of 35°N are imposed in the model. The combined effect of the zonal wind and PV gradient anomalies provide a refinement of the Francis and Vavrus (2012) argument.
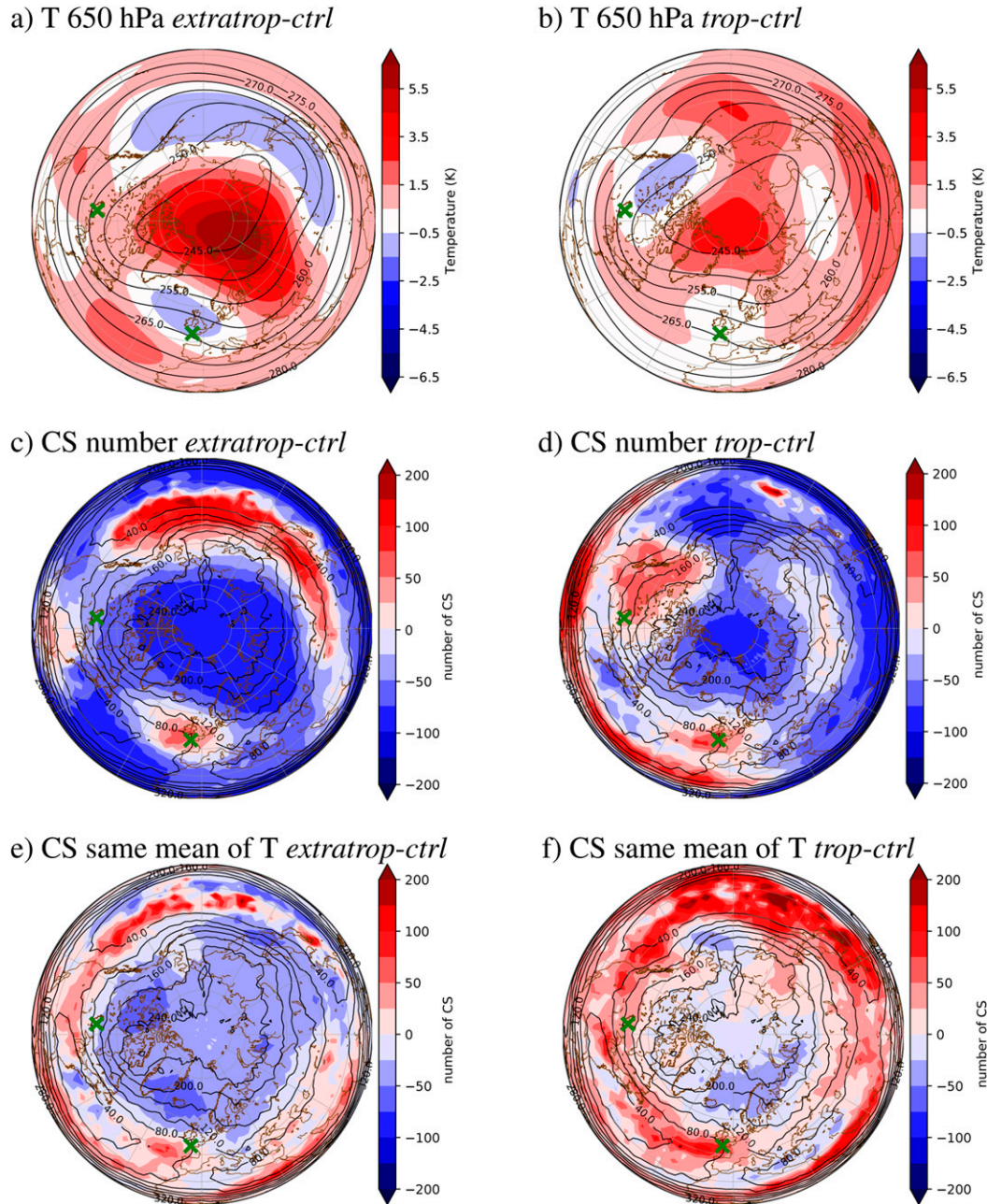
a) T 650 hPa *extratrop-ctrl*

b) T 650 hPa *trop-ctrl*

c) CS number *extratrop-ctrl*

d) CS number *trop-ctrl*

e) CS same mean of T *extratrop-ctrl*

f) CS same mean of T *trop-ctrl*

FIG. 9. (top) The 650-hPa temperature anomaly, as in Fig. 2b, but for (a) extratrop − ctrl difference and (b) trop − ctrl difference. (middle) CS number, as in Fig. 7a, but for (c) extratrop − ctrl difference and (d) trop − ctrl difference. (bottom) CS number with data translated to the same mean as in ctrl, as in Fig. 8b, but for (c) extratrop − ctrl difference and (d) trop − ctrl difference.

To be more precise, the increase in amplitude of slowly propagating waves is larger relative to the decrease of rapidly eastward-propagating waves. This effect appears to originate from the tropical anomalies present during the warm Arctic winters. When the model is forced to converge toward tropical anomalies only, it does indeed create a warm Arctic pattern—which confirms the findings by Baggett and Lee (2017) and Gong et al. (2020)—but additionally it shows a large increase in

slowly propagating wave energy similar to the full AA run. The reason for that behavior remains unclear.

We have also analyzed the impact of AA on cold spells (CS). CS are defined with a temperature threshold-based criterion, complemented by a duration criterion of at least 5 days. The increase of mean temperature has the obvious effect of decreasing on average the probability of passing the threshold, and hence decreases the average occurrence of CS.
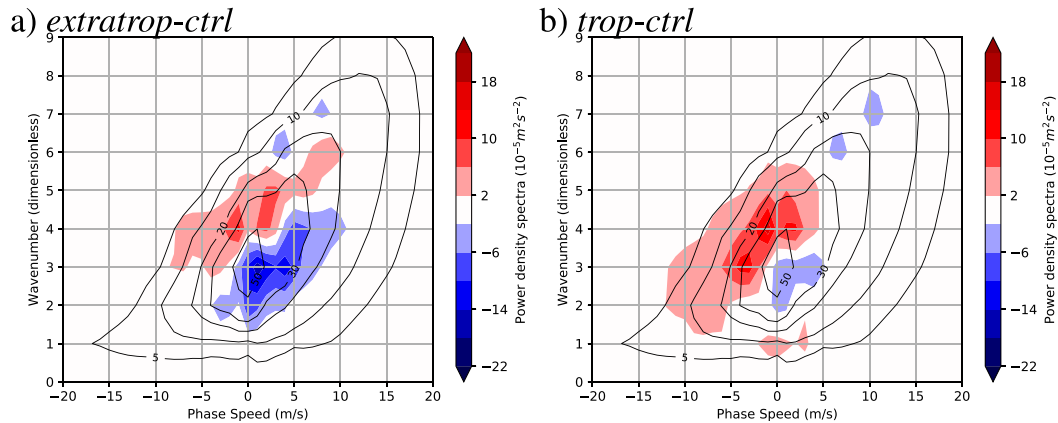
FIG. 10. As in Fig. 4, but for (a) extratrop − ctrl difference and (b) trop − ctrl difference.

Nevertheless, the local increase of low-frequency variability associated with the change of Rossby wave dynamics opposes in some regions the effect of the mean temperature increase. There is a compensation of the two effects in some midlatitude regions as in the northwestern Atlantic south of Greenland, which leaves the frequency of CS little changed. A net increase in CS frequency appears in regions of colder mean temperature. The increase over western Europe is largely due to the colder mean temperature but also slightly due to increase in the low-frequency variability. The increase in CS in the North American continental regions is more largely due to the increase in variability than to the colder mean temperature. Additionally, the increase in low-frequency variability explains why CS with duration longer than 5 days are more numerous. Numerical experiments comparing the response to different latitudinal bands of anomalies show that the increased number of CS is more due to the tropics than the mid- and high latitudes. This is consistent with the fact that the amplification of slowly varying waves is more important in the run where tropical anomalies are imposed.

Confirming the above results by looking at the observations of the real atmosphere is not an easy task. First, the real anomalies of the reanalysis data are small compared to those used to force the model. Remember that the warm winter forcing in the model is 2–3 times greater than that of the real data. Second, the observational period covers a much smaller period than that analyzed in the model and cannot provide robust statistical results. Third, our analysis is based on the composite of six very different seasons and the net effect might be small compared to individual seasons. Indeed, the recent review article of Cohen et al. (2020) shows that the observed large-scale anomalies linked to regionally localized Arctic anomalous warmings can be very different from one region to another. For example, the large-scale response of the Asian continental temperature to a heating of the Kara Sea or of the Greenland Sea can be opposed in sign. The response shown in the present work could consequently be real but not be the prevailing one.

Exploring each of these localized forcings and their causal relationship with different heating patterns in the tropics (which we found in the present paper to be important) can definitely be done in the present modeling framework. This would require a full study by itself which we reserve for future work. This would also help clarify whether global warming and other regional warmings, and not only anomalies setting the polar amplification pattern, could also induce a net change in Rossby wave phase speed.

APPENDIX

Temperature Computation in QG Model

The only free variable of the QG model is the QG potential vorticity q (or equivalently the streamfunction Ψ). Temperature can be diagnostically computed from it. Using Ψ and the Coriolis parameter f, the geopotential Φ satisfies the balance equation [see, e.g., Holton (2004) or any other geophysical fluid dynamics manual]:

$$\nabla^2 \Phi = \nabla \cdot (f \nabla \Psi) = \nabla f \cdot \nabla \Psi + f \nabla^2 \Psi. \quad \text{(A1)}$$

The Laplacian of the geopotential can then be integrated twice to get the geopotential. The computation of the geopotential consequently involves an arbitrary integration constant that corresponds to its spatial mean value.

The temperature between the levels is computed using two assumptions: the hydrostatic approximation and the law of perfect gas for air, which give

$$\delta\Phi = -R_{air} T \frac{\delta P}{P}. \qquad (A2)$$

And discretizing on the vertical axis of the model,

$$T_{12} = \frac{\Phi_1 - \Phi_2}{R_{air} \ln\left(\frac{P_2}{P_1}\right)}, \qquad (A3)$$

$$T_{23} = \frac{\Phi_2 - \Phi_3}{R_{air} \ln\left(\frac{P_3}{P_2}\right)}, \qquad (A4)$$

where T_{12} is the mean temperature between levels 1 (200 hPa) and 2 (500 hPa), which is at the mean pressure level 350 hPa; T_{23} is the mean temperature between levels 2 (500 hPa) and 3 (800 hPa), which is at the lower level 650 hPa; and R_{air} is the gas constant for dry air.

The temperature computed using this method depends on the arbitrary integration coefficient of Φ from the inversion of the horizontal Laplacian in Eq. (A1). To define this constant we proceed as follows: for the ctrl integration we chose the mean geopotential height of the U.S. standard atmosphere; for the AA integration we chose an ad hoc constant, so that the space-mean difference of temperature between the two integrations is the same of the two target climatologies (i.e., the map in color in Fig. 2a, and the equivalent map at 350 hPa). The maps in Figs. 2a and 2b, consequently, have the same global space mean by construction.

REFERENCES

Bader, J., M. D. S. Mesquita, K. I. Hodges, N. Keenlyside, S. Osterhus, and M. Miles, 2011: A review on Northern Hemisphere sea-ice, storminess and the North Atlantic oscillation: Observations and projected changes. *Atmos. Res.*, **101**, 809–834, https://doi.org/10.1016/j.atmosres.2011.04.007.

Baggett, C., and S. Lee, 2017: An identification of the mechanisms that lead to Arctic warming during planetary-scale and synoptic-scale wave life cycles. *J. Atmos. Sci.*, **74**, 1859–1877, https://doi.org/10.1175/JAS-D-16-0156.1.

Barnes, E. A., 2013: Revisiting the evidence linking Arctic amplification to extreme weather in midlatitudes. *Geophys. Res. Lett.*, **40**, 4734–4739, https://doi.org/10.1002/grl.50880.

——, and J. A. Screen, 2015: The impact of Arctic warming on the midlatitude jet-stream: Can it? Has it? Will it? *Wiley Interdiscip. Rev.: Climate Change*, **6**, 277–286, https://doi.org/10.1002/wcc.337.

——, E. Dunn-Sigouin, G. Masato, and T. Woollings, 2014: Exploring recent trends in Northern Hemisphere blocking. *Geophys. Res. Lett.*, **41**, 638–644, https://doi.org/10.1002/2013GL058745.

Binder, H., M. Boettcher, C. M. Grams, H. Joos, S. Pfahl, and H. Wernli, 2017: Exceptional air mass transport and dynamical drivers of an extreme wintertime Arctic warm event. *Geophys. Res. Lett.*, **44**, 12026–12036, https://doi.org/10.1002/2017GL075841.

Buehler, T., C. C. Raible, and T. F. Stocker, 2011: The relationship of winter season North Atlantic blocking frequencies to extreme cold and dry spells in the ERA-40. *Tellus*, **63A**, 212–222, https://doi.org/10.1111/j.1600-0870.2010.00492.x.

Butler, A. H., D. W. J. Thompson, and R. Heikes, 2010: The steady-state atmospheric circulation response to climate change–like thermal forcings in a simple general circulation model. *J. Climate*, **23**, 3474–3496, https://doi.org/10.1175/2010JCLI3228.1.

Cattiaux, J., R. Vautard, C. Cassou, P. Yiou, V. Masson-Delmotte, and F. Codron, 2010: Winter 2010 in Europe: A cold extreme in a warming climate. *Geophys. Res. Lett.*, **37**, L20704, https://doi.org/10.1029/2010GL044613.

——, Y. Peings, D. Saint-Martin, N. Trou-Kechout, and S. J. Vavrus, 2016: Sinuosity of midlatitude atmospheric flow in a warming world. *Geophys. Res. Lett.*, **43**, 8259–8268, https://doi.org/10.1002/2016GL070309.

Cohen, J., 2016: An observational analysis: Tropical relative to Arctic influence on midlatitude weather in the era of Arctic amplification. *Geophys. Res. Lett.*, **43**, 5287–5294, https://doi.org/10.1002/2016GL069102.

——, J. Foster, M. Barlow, K. Saito, and J. Jones, 2010: Winter 2009–2010: A case study of an extreme Arctic oscillation event. *Geophys. Res. Lett.*, **37**, L17707, https://doi.org/10.1029/2010GL044256.

——, J. C. Furtado, M. Barlow, V. A. Alexeev, and J. E. Cherry, 2012a: Arctic warming, increasing snow cover and widespread boreal winter cooling. *Environ. Res. Lett.*, **7**, 014007, https://doi.org/10.1088/1748-9326/7/1/014007.

——, ——, ——, ——, and ——, 2012b: Asymmetric seasonal temperature trends. *Geophys. Res. Lett.*, **39**, L04705, https://doi.org/10.1029/2011GL050582.

——, and Coauthors, 2014: Recent Arctic amplification and extreme mid-latitude weather. *Nat. Geosci.*, **7**, 627–637, https://doi.org/10.1038/ngeo2234.

——, and Coauthors, 2018: Arctic change and possible influence on mid-latitude climate and weather. U.S. CLIVAR Rep., 45 pp.

——, and Coauthors, 2020: Divergent consensuses on Arctic amplification influence on midlatitude severe winter weather. *Nat. Climate Change*, **10**, 20–29, https://doi.org/10.1038/s41558-019-0662-y.

Corti, S., A. Giannini, S. Tibaldi, and F. Molteni, 1997: Patterns of low-frequency variability in a three-level quasi-geostrophic model. *Climate Dyn.*, **13**, 883–904, https://doi.org/10.1007/s003820050203.

Coumou, D., V. Petoukhov, S. Rahmstorf, S. Petri, and H. J. Schellnhuber, 2014: Quasi-resonant circulation regimes and hemispheric synchronization of extreme weather in boreal summer. *Proc. Natl. Acad. Sci. USA*, **111**, 12 331–12 336, https://doi.org/10.1073/pnas.1412797111.

——, J. Lehmann, and J. Beckmann, 2015: The weakening summer circulation in the Northern Hemisphere mid-latitudes. *Science*, **348**, 324–327, https://doi.org/10.1126/science.1261768.

D'Andrea, F., and R. Vautard, 2000: Reducing systematic errors by empirically correcting model errors. *Tellus*, **52A**, 21–41, https://doi.org/10.3402/tellusa.v52i1.12251.

——, and ——, 2001: Extratropical low-frequency variability as a low dimensional problem I: A simplified model. *Quart. J. Roy. Meteor. Soc.*, **127**, 1357–1374, https://doi.org/10.1002/qj.49712757413.

Davini, P., and F. D'Andrea, 2020: From CMIP3 to CMIP6: Northern Hemisphere atmospheric blocking simulation in present and future climate. *J. Climate*, **33**, 10 021–10 038, https://doi.org/10.1175/JCLI-D-19-0862.1.

——, C. Cagnazzo, S. Gualdi, and A. Navarra, 2012: Bidimensional diagnostics, variability, and trends of Northern Hemisphere blocking. *J. Climate*, **25**, 6496–6509, https://doi.org/10.1175/JCLI-D-12-00032.1.

Dee, D. P., and Coauthors, 2011: The ERA-Interim reanalysis: Configuration and performance of the data assimilation system. *Quart. J. Roy. Meteor. Soc.*, **137**, 553–597, https://doi.org/10.1002/qj.828.

Dell'Aquila, A., V. Lucarini, P. M. Ruti, and S. Calmanti, 2005: Hayashi spectra of the Northern Hemisphere mid-latitude atmospheric variability in the NCEP–NCAR and ECMWF reanalyses. *Climate Dyn.*, **25**, 639–652, https://doi.org/10.1007/s00382-005-0048-x.

Di Capua, G., and D. Coumou, 2016: Changes in meandering of the Northern Hemisphere circulation. *Environ. Res. Lett.*, **11**, 094028, https://doi.org/10.1088/1748-9326/11/9/094028.

Drouard, M., G. Rivière, and P. Arbogast, 2013: The North Atlantic Oscillation response to large-scale atmospheric anomalies in the northeastern Pacific. *J. Atmos. Sci.*, **70**, 2854–2874, https://doi.org/10.1175/JAS-D-12-0351.1.

Fletcher, T., L. Warden, J. Sinninghe-Damste, K. J. Brown, N. Rybcynski, J. Gosse, and A. Ballantyne, 2019: Evidence for fire in the Pliocene Arctic in response to amplified temperature. *Climate Past*, **15**, 1063–1081, https://doi.org/10.5194/cp-15-1063-2019.

Francis, J. A., and S. J. Vavrus, 2012: Evidence linking Arctic amplification to extreme weather in mid-latitudes. *Geophys. Res. Lett.*, **39**, L06801, https://doi.org/10.1029/2012GL051000.

Fromang, S., and G. Rivière, 2020: The effect of the Madden–Julian oscillation on the North Atlantic Oscillation using idealized numerical experiments. *J. Atmos. Sci.*, **77**, 1613–1635, https://doi.org/10.1175/JAS-D-19-0178.1.

Gao, Y., L. R. Leung, J. Lu, and G. Masato, 2015: Persistent cold air outbreaks over North America in a warming climate. *Environ. Res. Lett.*, **10**, 044001, https://doi.org/10.1088/1748-9326/10/4/044001.

Gong, T., S. B. Feldstein, and S. Lee, 2017: The role of downward infrared radiation in the recent Arctic winter warming trend. *J. Climate*, **30**, 4937–4949, https://doi.org/10.1175/JCLI-D-16-0180.1.

——, ——, and ——, 2020: Rossby wave propagation from the Arctic into midlatitudes: Does it arise from in-situ latent heating or a trans-Arctic wave train? *J. Climate*, **33**, 3619–3633, https://doi.org/10.1175/JCLI-D-18-0780.1.

Graversen, R. G., and M. Wang, 2009: Polar amplification in a coupled climate model with locked albedo. *Climate Dyn.*, **33**, 629–643, https://doi.org/10.1007/s00382-009-0535-6.

Grotjahn, R., and Coauthors, 2016: North American extreme temperature events and related large scale meteorological patterns: A review of statistical methods, dynamics, modeling and trends. *Climate Dyn.*, **46**, 1151–1184, https://doi.org/10.1007/s00382-015-2638-6.

Harnik, N., G. Messori, R. Caballero, and S. B. Feldstein, 2016: The circumglobal North American wave pattern and its relation to cold events in eastern North America. *Geophys. Res. Lett.*, **43**, 11015–11023, https://doi.org/10.1002/2016GL070760.

Hassanzadeh, P., Z. Kuang, and B. F. Farrell, 2014: Responses of midlatitude blocks and wave amplitude to changes in the meridional temperature gradient in an idealized dry GCM. *Geophys. Res. Lett.*, **41**, 5223–5232, https://doi.org/10.1002/2014GL060764.

Hayashi, Y., 1971: A generalized method of resolving disturbances into progressive and retrogressive waves by space Fourier and time cross-spectral analyses. *J. Meteor. Soc. Japan*, **49**, 125–128, https://doi.org/10.2151/jmsj1965.49.2_125.

——, 1979: A generalized method of resolving transient disturbances into standing and traveling waves by space-time spectral analysis. *J. Atmos. Sci.*, **36**, 1017–1029, https://doi.org/10.1175/1520-0469(1979)036<1017:AGMORT>2.0.CO;2.

——, 1982: Space-time spectral analysis and its applications to atmospheric waves. *J. Meteor. Soc. Japan*, **60**, 156–171, https://doi.org/10.2151/jmsj1965.60.1_156.

Held, I. M., 1983: Stationary and quasi-stationary eddies in the extratropical troposphere: Theory. *Large-Scale Dynamical Processes in the Atmosphere*, R. P. Pearce and B. J. Hoskins, Eds., Academic Press, 127–168.

Hell, M. C., T. Schneider, and C. Li, 2020: Atmospheric circulation response to short-term Arctic warming in an idealized model. *J. Atmos. Sci.*, **77**, 531–549, https://doi.org/10.1175/JAS-D-19-0133.1.

Holton, J. R., 2004: *An Introduction to Dynamic Meteorology*. 4th ed. International Geophysics Series, Elsevier, 535 pp.

Honda, M., J. Inoue, and S. Yamane, 2009: Influence of low Arctic sea-ice minima on anomalously cold Eurasian winters. *Geophys. Res. Lett.*, **36**, L08707, https://doi.org/10.1029/2008GL037079.

Hoskins, B. J., and D. J. Karoly, 1981: The steady linear response of a spherical atmosphere to thermal and orographic forcing. *J. Atmos. Sci.*, **38**, 1179–1196, https://doi.org/10.1175/1520-0469(1981)038<1179:TSLROA>2.0.CO;2.

——, and T. Ambrizzi, 1993: Rossby wave propagation on a realistic longitudinally varying flow. *J. Atmos. Sci.*, **50**, 1661–1671, https://doi.org/10.1175/1520-0469(1993)050<1661:RWPOAR>2.0.CO;2.

——, and T. Woollings, 2015: Persistent extratropical regimes and climate extremes. *Curr. Climate Change Rep.*, **1**, 115–124, https://doi.org/10.1007/s40641-015-0020-8.

Hurrell, J. W., 1995: Decadal trends in the North Atlantic Oscillation: Regional temperatures and precipitation. *Science*, **269**, 676–679, https://doi.org/10.1126/science.269.5224.676.

Inoue, J., and M. E. Hori, 2011: Arctic cyclogenesis at the marginal ice zone: A contributory mechanism for the temperature amplification? *Geophys. Res. Lett.*, **38**, L12502, https://doi.org/10.1029/2011GL047696.

Kug, J.-S., J.-H. Jeong, Y.-S. Jang, B.-M. Kim, C. K. Folland, S.-K. Min, and S.-W. Son, 2015: Two distinct influences of Arctic warming on cold winters over North America and East Asia. *Nat. Geosci.*, **8**, 759–762, https://doi.org/10.1038/ngeo2517.

Lee, M.-Y., C.-C. Hong, and H.-H. Hsu, 2015: Compounding effects of warm sea surface temperature and reduced sea ice on the extreme circulation over the extratropical North Pacific and North America during the 2013–2014 boreal winter. *Geophys. Res. Lett.*, **42**, 1612–1618, https://doi.org/10.1002/2014GL062956.

Lee, S., T. Gong, N. Johnson, S. B. Feldstein, and D. Polland, 2011: On the possible link between tropical convection and the Northern Hemisphere Arctic surface air temperature change between 1958 and 2001. *J. Climate*, **24**, 4350–4367, https://doi.org/10.1175/2011JCLI4003.1.

——, ——, S. B. Feldstein, J. A. Screen, and I. Simmonds, 2017: Revisiting the cause of the 1989–2009 Arctic surface warming using the surface energy budget: Downward infrared radiation dominates the surface fluxes. *Geophys. Res. Lett.*, **44**, 10 654–10 661, https://doi.org/10.1002/2017GL075375.

Liu, J., J. A. Curry, H. Wang, M. Song, and R. M. Horton, 2012: Impact of declining Arctic sea ice on winter snowfall. *Proc. Natl. Acad. Sci. USA*, **109**, 4074–4079, https://doi.org/10.1073/pnas.1114910109.

Lu, J., and M. Cai, 2009: Seasonality of polar surface warming amplification in climate simulations. *Geophys. Res. Lett.*, **36**, L16704, https://doi.org/10.1029/2009GL040133.

Mann, M. E., S. Rahmstorf, K. Kornhuber, B. A. Steinman, S. K. Miller, S. Petri, and D. Coumou, 2018: Projected changes in persistent extreme summer weather events: The role of quasi-resonant amplification. *Sci. Adv.*, **4**, eaat3272, https://doi.org/10.1126/sciadv.aat3272.

Marshall, J., and F. Molteni, 1993: Toward a dynamical understanding of planetary-scale flow regimes. *J. Atmos. Sci.*, **50**, 1792–1818, https://doi.org/10.1175/1520-0469(1993)050<1792:TADUOP>2.0.CO;2.

Masato, G., B. J. Hoskins, and T. Woollings, 2013: Winter and summer Northern Hemisphere blocking in CMIP5 models. *J. Climate*, **26**, 7044–7059, https://doi.org/10.1175/JCLI-D-12-00466.1.

Messori, G., R. Caballero, and M. Gaetani, 2016: On cold spells in North America and storminess in western Europe. *Geophys. Res. Lett.*, **43**, 6620–6628, https://doi.org/10.1002/2016GL069392.

——, C. Woods, and R. Caballero, 2018: On the drivers of wintertime temperature extremes in the high Arctic. *J. Climate*, **31**, 1597–1618, https://doi.org/10.1175/JCLI-D-17-0386.1.

Mori, M., M. Watanabe, H. Shiogama, J. Inoue, and M. Kimoto, 2014: Robust Arctic sea-ice influence on the frequent Eurasian cold winters in past decades. *Nat. Geosci.*, **7**, 869–873, https://doi.org/10.1038/ngeo2277.

Nakamura, T., K. Yamazaki, K. Iwamoto, M. Honda, Y. Miyoshi, Y. Ogawa, and J. Ukita, 2015: A negative phase shift of the winter AO/NAO due to the recent Arctic sea-ice reduction in late autumn. *J. Geophys. Res. Atmos.*, **120**, 3209–3227, https://doi.org/10.1002/2014JD022848.

Overland, J. E., and M. Wang, 2005: The Arctic climate paradox: The recent decrease of the Arctic Oscillation. *Geophys. Res. Lett.*, **32**, L06701, https://doi.org/10.1029/2004GL021752.

——, K. R. Wood, and M. Wang, 2011: Warm Arctic–cold continents: Climate impacts of the newly open Arctic Sea. *Polar Res.*, **30**, 15787, https://doi.org/10.3402/polar.v30i0.15787.

Peings, Y., and G. Magnusdottir, 2014: Response of the wintertime Northern Hemisphere atmospheric circulation to current and projected Arctic sea ice decline: A numerical study with CAM5. *J. Climate*, **27**, 244–264, https://doi.org/10.1175/JCLI-D-13-00272.1.

Petoukhov, V., and V. A. Semenov, 2010: A link between reduced Barents-Kara sea ice and cold winter extremes over northern continents. *J. Geophys. Res.*, **115**, D21111, https://doi.org/10.1029/2009JD013568.

Pithan, F., and T. Mauritsen, 2014: Arctic amplification dominated by temperature feedbacks in contemporary climate models. *Nat. Geosci.*, **7**, 181–184, https://doi.org/10.1038/ngeo2071.

Riboldi, J., F. Lott, F. d'Andrea, and G. Rivière, 2020: On the linkage between Rossby wave phase speed, atmospheric blocking, and Arctic amplification. *Geophys. Res. Lett.*, **47**, e2020GL087796, https://doi.org/10.1029/2020GL087796.

Rinke, A., M. Maturilli, R. M. Graham, H. Matthes, D. Handorf, L. Cohen, S. R. Hudson, and J. C. Moore, 2017: Extreme cyclone events in the Arctic: Wintertime variability and trends. *Environ. Res. Lett.*, **12**, 094006, https://doi.org/10.1088/1748-9326/aa7def.

Rivière, G., 2011: A dynamical interpretation of the poleward shift of the jet streams in global warming scenarios. *J. Atmos. Sci.*, **68**, 1253–1272, https://doi.org/10.1175/2011JAS3641.1.

——, and M. Drouard, 2015: Understanding the contrasting North Atlantic Oscillation anomalies of the winters of 2010 and 2014. *Geophys. Res. Lett.*, **42**, 6868–6875, https://doi.org/10.1002/2015GL065493.

Robert, L., G. Rivière, and F. Codron, 2019: Effect of upper- and lower-level baroclinicity on the persistence of the leading mode of midlatitude jet variability. *J. Atmos. Sci.*, **76**, 155–169, https://doi.org/10.1175/JAS-D-18-0010.1.

Ronalds, B., E. Barnes, and P. Hassanzadeh, 2018: A barotropic mechanism for the response of jet stream variability to Arctic amplification and sea ice loss. *J. Climate*, **31**, 7069–7085, https://doi.org/10.1175/JCLI-D-17-0778.1.

Santer, B. D., and Coauthors, 2018: Consistency of modeled and observed temperature trends in the tropical troposphere. *Climate Modelling: Philosophical and Conceptual Issues*, E. A. Lloyd and E. Winsberg, Eds., Palgrave Macmillan, 85–136, https://doi.org/10.1007/978-3-319-65058-6_5.

Schneider, T., T. Bischoff, and H. Płotka, 2015: Physics of changes in synoptic midlatitude temperature variability. *J. Climate*, **28**, 2312–2331, https://doi.org/10.1175/JCLI-D-14-00632.1.

Screen, J. A., 2014: Arctic amplification decreases temperature variance in northern mid- to high-latitudes. *Nat. Climate Change*, **4**, 577–582, https://doi.org/10.1038/nclimate2268.

——, and I. Simmonds, 2010: The central role of diminishing sea ice in recent Arctic temperature amplification. *Nature*, **464**, 1334–1337, https://doi.org/10.1038/nature09051.

——, and ——, 2013: Exploring links between Arctic amplification and mid-latitude weather. *Geophys. Res. Lett.*, **40**, 959–964, https://doi.org/10.1002/grl.50174.

Serreze, M. C., and R. Barry, 2011: Processes and impacts of Arctic amplification: A research synthesis. *Global Planet. Change*, **77**, 85–96, https://doi.org/10.1016/j.gloplacha.2011.03.004.

——, A. P. Barrett, J. C. Stroeve, D. N. Kindig, and M. M. Holland, 2009: The emergence of surface-based Arctic amplification. *Cryosphere*, **3**, 11–19, https://doi.org/10.5194/tc-3-11-2009.

Shaw, T. A., and Coauthors, 2016: Storm track processes and the opposing influences of climate change. *Nat. Geosci.*, **9**, 656–664, https://doi.org/10.1038/ngeo2783.

Sun, L., J. Perlwitz, and M. Hoerling, 2016: What caused the recent "warm Arctic, cold continents" trend pattern in winter temperatures? *Geophys. Res. Lett.*, **43**, 5345–5352, https://doi.org/10.1002/2016GL069024.

Tamarin-Brodsky, T., K. Hodges, B. J. Hoskins, and T. G. Shepherd, 2019: A dynamical perspective on atmospheric temperature variability and its response to climate change. *J. Climate*, **32**, 1707–1724, https://doi.org/10.1175/JCLI-D-18-0462.1.

Thompson, D. W. J., and J. M. Wallace, 1998: The Arctic Oscillation signature in the wintertime geopotential height and temperature fields. *Geophys. Res. Lett.*, **25**, 1297–1300, https://doi.org/10.1029/98GL00950.

Wallace, J. M., I. M. Held, D. W. J. Thompson, K. E. Trenberth, and J. E. Walsh, 2014: Global warming and winter weather. *Science*, **343**, 729–730, https://doi.org/10.1126/science.343.6172.729.

Woods, C., and R. Caballero, 2016: The role of moist intrusions in winter Arctic warming and sea ice decline. *J. Climate*, **29**, 4473–4485, https://doi.org/10.1175/JCLI-D-15-0773.1.

Yang, X.-Y., X. Yuan, and M. Ting, 2016: Dynamical link between the Barents–Kara sea ice and the Arctic Oscillation. *J. Climate*, **29**, 5103–5122, https://doi.org/10.1175/JCLI-D-15-0669.1.

Yiou, P., and M. Nogaj, 2004: Extreme climatic events and weather regimes over the North Atlantic: When and where? *Geophys. Res. Lett.*, **31**, L07202, https://doi.org/10.1029/2003GL019119.